Engineering Failure Analysis 163 (2024) 108530

Contents lists available at ScienceDirect

Engineering Failure Analysis

journal homepage: www.elsevier.com/locate/engfailanal

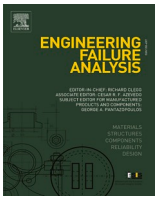

A comparison of vintage and modern X65 pipeline steel using hollow specimen technique for in-situ hydrogen testing

Alessandro Campari [a,*], Florian Konert [b], Oded Sobol [b], Antonio Alvaro [c]

[a] Department of Mechanical and Industrial Engineering, Norwegian University of Science and Technology NTNU, Richard Birkelands vei 2b, Trondheim 7034, Norway
[b] Department of Component Safety, Bundesanstalt für Materialforschung und -prüfung BAM, Unter den Eichen 87, Berlin 12205, Germany
[c] Department of Materials and Nanotechnology, SINTEF Industry, Richard Birkelands vei 2b, Trondheim 7034, Norway

ARTICLE INFO

Keywords:
Mechanical engineering
Hydrogen pipelines
Ferritic steel
Mechanical testing
Hydrogen embrittlement
Material compatibility

ABSTRACT

The transition toward a hydrogen-based economy requires a widespread transport and distribution network, and repurposed natural gas pipelines are a viable option. An assessment of the hydrogen-induced degradation of pipeline steels is needed to inject H_2 gas into the existing infrastructure safely. The conservative and standardized method consists of in-situ tensile tests in an autoclave filled with high-pressure hydrogen gas. A proposed alternative method involves using a hollow specimen as containment volume and applying the gas pressure in the inner cavity. This technique has lower costs and shorter test preparation time but is not standardized yet. This study aims to evaluate and compare the tensile properties of API 5L X65 pipeline steel in two states: vintage and modern. The influence of the surface roughness is investigated through parallel tests with drilled and reamed specimens. Hydrogen tests are compared with reference tests in an inert environment. A significant hydrogen-induced decrease in tensile properties is observed, and no significant difference between vintage and modern X65 can be drawn. The reduction in tensile properties is more significant in specimens with higher inner surface roughness. The evaluation of surface conditions appears crucial when assessing the HE susceptibility of hydrogen transport and storage equipment.

1. Introduction

The European Commission recognized hydrogen as a clean and versatile energy carrier with the potential to decarbonize transport, power production, and other industrial sectors. The EU Hydrogen Strategy [1] was implemented in national and regional roadmaps in different countries to guide the future rollout of hydrogen-based technologies. Despite the great interest of industries, governments, and researchers in green hydrogen, this sustainable energy carrier is not devoid of safety concerns. Hydrogen atoms can diffuse into most structural materials and degrade their mechanical properties to an extent that can result in early failures of industrial equipment [2]. Although hydrogen-induced damages have been widely investigated, the underlying mechanisms remain debated. Therefore, further research is required to assess the hydrogen compatibility of base materials and weld joints [3].

Hydrogen embrittlement (HE) is a long-known phenomenon that results from the synergy of three factors: hydrogen-containing environment, susceptible material, and mechanical load [4]. Hydrogen atoms from the operating environment, cathodic protection,

* Corresponding author.
E-mail address: alessandro.campari@ntnu.no (A. Campari).

https://doi.org/10.1016/j.engfailanal.2024.108530
Received 17 February 2024; Received in revised form 7 May 2024; Accepted 3 June 2024
Available online 5 June 2024

manufacturing processes, or corrosion mechanisms can enter the metal lattice, permeate through the bulk material, and get trapped in different locations. The material's microstructure, along with temperature, strongly influences the diffusivity and, therefore, the steel's compatibility with hydrogen environments [5]. Hydrogen atoms can get trapped in vacancies, dislocations, grain boundaries, and non-metallic inclusions and escape from these sites only if their energy level is higher than the binding energy of the trap [6]. Diffusible hydrogen is responsible for the degradation of mechanical properties associated with hydrogen embrittlement [7], and the specific mechanism for low-alloy structural steels most likely results from the combination of hydrogen-enhanced decohesion (HEDE) and hydrogen-enhanced localized plasticity (HELP) [8].

When it comes to the qualification of industrial equipment, a limited number of codes are currently used to design components for hydrogen service. The most known are the ASME B31.12 [9], the standard for hydrogen pipes and pipelines, and the ASME BPVC-VIII-3 [10], which establishes the construction rules for high-pressure storage tanks. Both indicate the requirements for material compatibility with hydrogen based on the assessment of their fracture properties. This regulatory framework may impose over-conservative design criteria and a limited variety of high-performance materials for hydrogen handling and storage equipment. Therefore, new standards are required to regulate components' design, inspection, and maintenance. Repurposing natural gas pipelines for hydrogen transport is even more challenging when assessing the hydrogen compatibility of vintage steels. Most of this infrastructure is designed according to engineering standards that do not address hydrogen transport, as in the case of the subsea pipelines on the Norwegian continental shelf, designed according to the code DNV-ST-F101 [11]. In addition, evaluating the pipeline conditions after a long service in aggressive environments is crucial since various surface defects (such as corrosion, dents, and scratches) can affect their structural integrity. Corrosion defects represent preferential sites to accumulate H atoms and initiate hydrogen-induced cracks [12], while dents are particularly susceptible to HE due to the high hydrostatic stress [13].

When assessing the hydrogen impact on structural materials through tensile tests, two main categories of environmental conditions are commonly employed and can be found in the standards. The first involves testing in a H_2-rich environment, applying tensile stress concurrently with hydrogen exposure. The second entails testing in an ambient atmosphere after precharging with hydrogen. The former category, defined as in-situ testing, is required for carbon and low-alloy steels due to the high diffusivity of hydrogen atoms (greater than 10^{-10} m^2/s [14]). In fact, a significant amount of hydrogen can escape the material between precharging and test completion. Hydrogen charging, whether in-situ or ex-situ, can be achieved through electrochemical or high-pressure gas charging [15]. The former method is simpler and emulates the cathodic protection in subsea pipelines. Conversely, charging with gaseous hydrogen mimics the conditions of H_2 transport and storage equipment (e.g., tanks and pipes) [14]. Many investigations use electrochemical charging and draw general conclusions about the impact of hydrogen; however, in some case, these charging methods cannot be compared one-to-one.

A well-established method to evaluate the influence of gaseous hydrogen on mechanical properties consists of testing in-situ in an autoclave filled with pressurized H_2 [16,17]. This technique is standardized in ASTM G142-98 [16] and ISO 11114–4 [17] and used for many structural materials. The most conservative process requires slow strain rate tensile (SSRT) tests, commonly used as a screening method to assess the hydrogen influence on material properties. These tests should simulate the operating conditions of industrial components and be reliable, affordable, and safe. Performing the tests in the autoclave allows for adjusting several parameters (e.g., pressure, temperature, oxygen content, and nominal strain rate). This degree of freedom allows to emulate the operating conditions of industrial components, which undergo tension when exposed to pressurized hydrogen gas. Despite these advantages, autoclave tests have long overall durations and high costs due to the strict safety regulations imposed by the relatively large amount of compressed gaseous hydrogen (CGH_2). This complex procedure can be performed only by a few laboratories worldwide, limiting the testing capacity and slowing down the development of new engineering standards for hydrogen technologies. A testing method that has been getting increasing attention in the last decades since it can provide safe and fast results consists of using hollow specimens with the inner surface exposed to pressurized hydrogen [18]. This technique requires a smaller amount of H_2 gas, achieves the safety requirements to perform such tests in laboratories, and can be adjusted into regular testing machines with minimal modifications for clamping the samples. However, tests with hollow samples are not yet standardized, and it is not clearly and fully understood how to compare results obtained by these different testing techniques [19].

In the past years, only a limited number of studies have investigated the effects of HE through hollow specimens. It was initially adopted to test the impact of hydrogen at cryogenic temperatures. Ogata [20,21] investigated the hydrogen compatibility of several austenitic steels by comparing three machining techniques (i.e., electric discharge, wire-cut, and honing), resulting in different inner surface roughness. A comparable test setup was used to assess the fatigue performance of other stainless steels at extremely low temperatures and elevated pressures, reaching 20 K and 70 MPa [22–26]. In addition, Ogata [27] explored the fatigue and tensile properties of stainless steels at temperatures up to 800 K, yielding results closely aligned with conventional tests. In pursuit of standardizing this method, Ogata and Ono [28] assessed the influence of inner surface roughness on SSRT test results for 316 and SNCM439 steels by comparing wire-cut, honed, and polished specimens. They proved how polished specimens were more sensitive to environmental changes. Michler et al. [29] examined several austenitic steels' yield and ultimate tensile strengths, drawing parallels between hollow and conventional specimens.

Only in recent years has the hollow specimen technique been used to evaluate the hydrogen compatibility of pipeline steels. Boot et al. [30] and Faucon et al. [31] developed a testing apparatus to assess the tensile properties and fatigue performance of base metal and welds of an X60 pipeline steel, varying the hydrogen pressure within the cavity. They highlighted the necessity to re-evaluate the welding defects before using the existing pipelines for hydrogen transport. Simultaneously, Michler et al. [8,23] explored the role of purge cycles in achieving the desired hydrogen purity within the hole and compared test results with solid specimens. Konert et al. [32] recently investigated the impact of gaseous hydrogen on the tensile properties of an X65 steel, visualizing the crack formation and growth through μCT imaging. In addition, Konert et al. [33] evaluated the tensile properties of vintage pipeline steel in CGH_2

environments, observing a significant ductility loss and quasi-cleavage fracture surface near the inner hole of the specimens. As shown, the utilization of hollow specimens is gaining increasing interest among the scientific community, and further research aims to standardize this testing technique in the coming years.

While most of the existing studies investigated the effects of temperature, pressure, and inner surface roughness in austenitic steels or the influence of pressure and hydrogen purity in pipeline steels, this research compares the hydrogen-induced reduction in tensile properties in API 5L X65 pipeline steel in two different states (i.e., vintage and modern) with various microstructures. Hollow specimens were tested in compressed H_2 gas and an inert reference environment (i.e., compressed argon). Pressure, temperature, and nominal strain rate were kept the same for all the tests. In contrast, two manufacturing techniques (i.e., drilling and reaming), resulting in different surface roughness, were used to produce the inner hole and evaluate the influence of surface finishing on the degradation of tensile properties. The specific impact of surface roughness on HE susceptibility remains relatively unexplored and has never been investigated in pipeline steels using this technique. Notches and grooves produced by the drilling process can act as crack initiation sites in hydrogen environments, constituting preferential paths for hydrogen uptake into the bulk material and accelerating the failure. Therefore, a deeper understanding of this critical factor could facilitate targeted mitigation strategies, enhancing the durability and reliability of hydrogen transport infrastructure. The severity of HE was quantified by determining the embrittlement index and the relative elongation loss. In addition, analysis of the microstructure, characterization of the materials, and post-mortem fractographic analysis allowed to clarify the failure mechanism.

2. Materials and methods

This study investigates two different pipeline legs made of API 5L X65 steel. This low-alloy steel has been used as a structural material for pipelines for decades and constitutes roughly 7 % of the European natural gas transport network [34]. Depending on the year of production and the manufacturing technique, components of the same steel grade exhibit different compositions and microstructures. For this reason, an X65 steel manufactured in 1982 by Fukuyama Steel Works and used since 1985 for natural gas transport was deemed representative of vintage pipeline steels. The material was extracted from the base metal of the inner pipe (770 mm in diameter, 26 mm thick, and 1 m long) in the longitudinal direction. The choice of this position is justified by the tests conducted on the same material by Myhre et al. [35], who showed how the specimens extracted from the mid-base metal manifested the highest hydrogen-induced ductility loss. This stretch of pipe is produced by rolling and forming through the UOE method (U-bending, O-bending, welding, and expanding) and longitudinally welded.

Similarly, a modern X65 steel manufactured in 2020 by Eisenbau Krämer was used as a comparison. The material was extracted from a pipe with an outer diameter of 610 mm, thickness of 28.6 mm, and 12.15 m long. The specimens were machined from the mid-base metal in the longitudinal direction to allow a direct comparison with the vintage X65. The pipe is welded with longitudinal submerged arc welding. The chemical compositions obtained through Spectrotest Optical Emission Spectroscopy (SPECTRO GmbH, Germany) for vintage and modern steels are reported in Table 1. The measured values are compared with the chemical compositions of the product specification levels (PLS) in API 5L [36].

The mechanical properties of the vintage steel were evaluated with tensile tests conducted in the air at room temperature, with a nominal strain rate of $2.5 \times 10^{-4}\ s^{-1}$. The average yield strength (YS), i.e., the nominal stress that will result in a plastic strain of 0.2 %, and the average ultimate tensile strength (UTS), i.e., the maximum nominal stress the material can withstand before breaking, were considered. In addition, minimum and maximum values of YS and UTS for an API 5L X65 steel are provided by the manufacturers and reported in Table 2.

The metal surfaces were treated by Nital etching for a microstructural analysis of the X65 pipeline steels. The microstructure of the X65 vintage steel is shown in Fig. 1a. It consists of polygonal ferrite and pearlite in banded appearance, with plate-like bainitic bands. The fraction of ferrite is approximately 83 % of the total, while the fraction of pearlite and bainite accounts for the remaining 17 %. The average grain size was determined through the average grain intercept (AGI) method and is approximately 4.2 μm. Fig. 1b shows the microstructure of the modern X65 steel. In contrast to the vintages steel, the modern X65 is characterized by a homogenous appearance, without bands. As with the vintage material, the microstructure mainly consists of ferrite grains with smaller fractions of bainite.

The axial hole was machined through two different techniques: conventional drilling with a high-speed steel (HSS) driller of 3 mm diameter and drilling with an HSS driller of 2.8 mm, followed by reaming to 3 mm diameter. Reaming after drilling allowed to obtain a smoother and more controlled inner surface. Drilled specimens have nominal average roughness (R_a) and a ten-point height of irregularities (R_z) of 1.5 μm and 8.5 μm, respectively. In comparison, reamed specimens have R_a and R_z equal to 0.1 μm and 1.4 μm, respectively. After the hole was produced, the outer geometry of all the specimens was manufactured by turning, and the outer surface was ground. The specimen's overall length and gauge length are 125.94 mm and 25.4 mm, respectively. The outer diameter is 6.35

Table 1
Measured and nominal chemical compositions of the API 5L X65 pipeline steels.

Chemical composition	C	Mn	P	S	Cr	Cu	Mo	Ni	Nb	V	Ti
Vintage measured	0.07	1.53	0.013	<0.002	0.02	<0.01	0.01	0.01	0.033	0.076	0.009
Modern measured	0.04	1.31	0.008	<0.002	0.05	0.02	0.21	0.44	<0.01	0.04	<0.01
PSL 1 nominal	≤0.28	≤1.4	≤0.03	≤0.03	≤0.50	≤0.50	≤0.50	≤0.50	≤0.05	≤0.05	≤0.05
PSL 2 nominal	0.18	1.70	0.025	0.015	≤0.50	≤0.50	≤0.50	≤0.50	≤0.05	≤0.05	≤0.05

Table 2
Yield and ultimate tensile strength of vintage and modern X65 pipeline steel in longitudinal direction.

	Measured YS	Minimum YS	Maximum YS	Measured UTS	Minimum UTS	Maximum UTS
Vintage X65	518 MPa	450 MPa	570 MPa	627 MPa	535 MPa	760 MPa
Modern X65	555 MPa	450 MPa	570 MPa	626 MPa	535 MPa	760 MPa

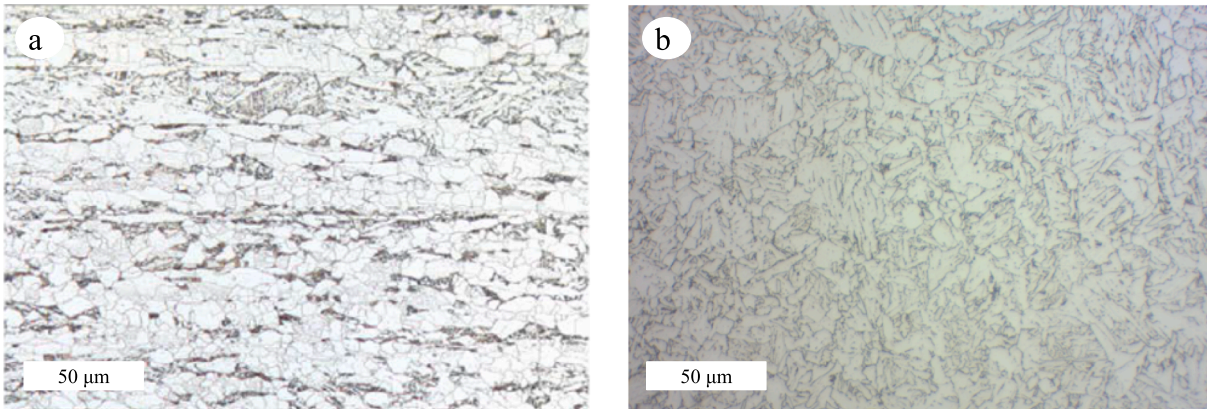

Fig. 1. Optical micrographs of the a) vintage X65 and b) modern X65 in the longitudinal direction.

mm. Fig. 2 shows the technical drawing of the specimen.

Slow strain rate tensile tests were performed using Grade 5.0 hydrogen (i.e., $H_2 \geq 99.999$ %, $O_2 \leq 2$ ppm, $H_2O \leq 3$ ppm, and $N_2 \leq 5$ ppm) and argon as a reference inert gas (Linde GmbH, Germany). H_2 gas was injected into the inner hole at a pressure of 6 MPa and at room temperature. The desired purity was obtained by six cycles of filling up to 6 MPa and venting down to 1 MPa, as described by Michler et al. [18]. The final oxygen content within the hollow specimen was estimated using Eq. (1), according to ANSI/CSA CHMC

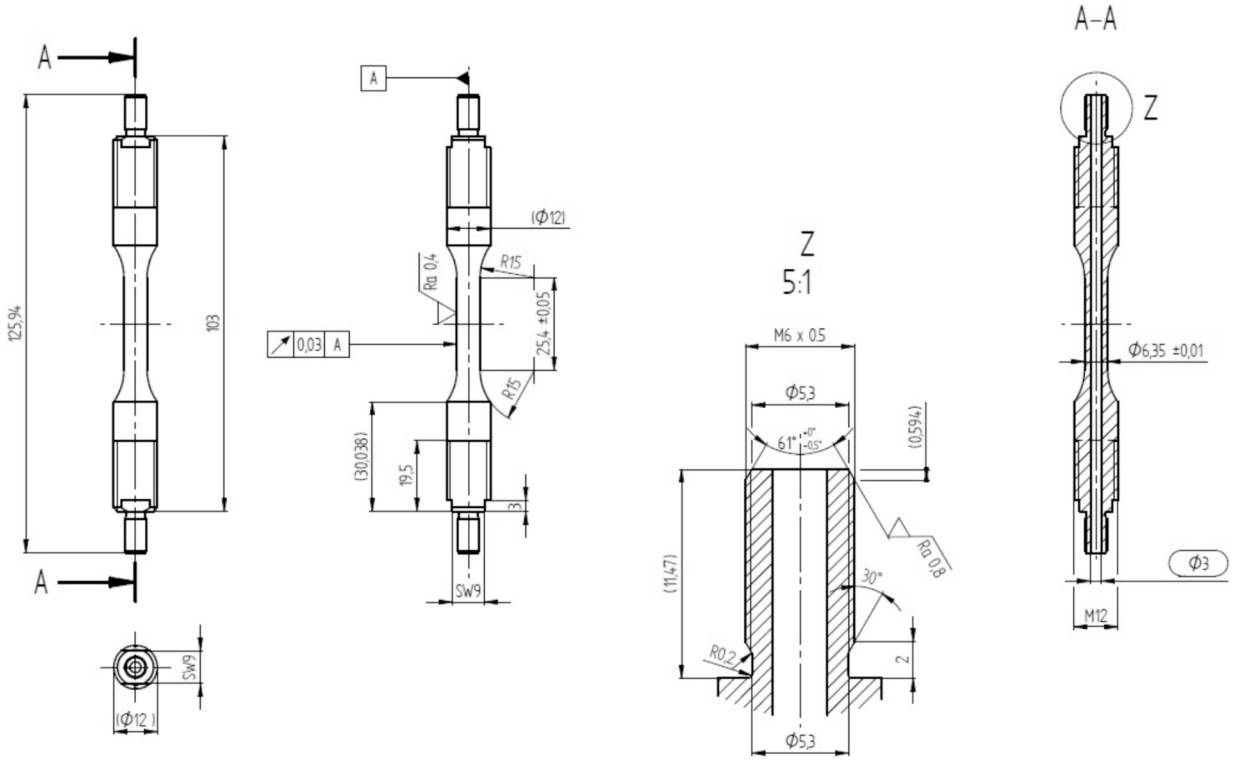

Fig. 2. Drawing and cross-section of the hollow specimen.

1–2014 [37]:

$$c_{final} = c_{initial} \cdot \left(\frac{p_{vent}}{p_{purge}}\right)^{n} \quad (1)$$

where $c_{initial}$ is the oxygen content in the air (i.e., 20.9 $\%_{vol}$), p_{vent} and p_{purge} are the venting and purging pressure, respectively (i.e., 1 and 6 MPa), and n is the number of purging cycles. All the tests were conducted at a nominal strain rate of 10^{-6} s^{-1}. The complete fracture of the specimens was considered the failure criterion. Even if pressure variations are negligible throughout the test duration, a pressure drop might occur before the complete fracture when the main crack reaches the outer surface of the specimen. The experimental setup is shown in Fig. 3. Additional components, such as hydrogen gas bottle, valves, and flexible hose, were integrated with a conventional 100 kN machine for SSRT tests (Cormet Testing Systems, Finland) in a standard laboratory environment at room temperature.

The embrittlement index (EI) is a key parameter for quantifying the effect of hydrogen on the material's tensile properties. It is defined in Eq. (2) as the relative change of reduced areas at fracture obtained in a hydrogen atmosphere and a reference environment (e.g., argon). The strain loss, defined in Eq. (3), allows for quantification of the relative reduction in elongation at failure after exposure to hydrogen-containing environments:

$$EI = \frac{RA_{Ar} - RA_{H_2}}{RA_{Ar}} \cdot 100 = \frac{\left[(A_o - A_f)/A_o\right]_{Ar} - \left[(A_o - A_f)/A_o\right]_{H_2}}{\left[(A_o - A_f)/A_o\right]_{Ar}} \cdot 100 \quad (2)$$

$$\varepsilon_{loss} = \frac{\varepsilon_{Ar} - \varepsilon_{H_2}}{\varepsilon_{Ar}} \cdot 100 = \frac{\left[(l_f - l_o)/l_o\right]_{Ar} - \left[(l_f - l_o)/l_o\right]_{H_2}}{\left[(l_f - l_o)/l_o\right]_{Ar}} \cdot 100 \quad (3)$$

where RA_{Ar} and RA_{H_2} represent the reduced areas in argon and hydrogen gas, respectively, A_o and A_f are the initial and final cross-sections, ε_{Ar} and ε_{H_2} are the strain at failure in argon and hydrogen gas, and l_o and l_f are the original gauge length and the gauge length at fracture, respectively. The initial cross-section and the original gauge length were obtained from the sketch in Fig. 2. It must be noted that the area of the hole was not counted as part of the cross-section, because the hole does not include any material that could be affected by hydrogen. The final fracture area was measured through a digital optical microscope Keyence VHX-5000. The post-mortem fractographic analysis was performed through a FEI Quanta 650 FEG scanning electron microscope (FEI Company, USA) with a high voltage of 20 kV for the vintage steel and a Phenom XL scanning electron microscope (Thermo-Fisher Phenom, Netherlands) with a second electron detector and a high voltage of 15 kV for the modern steel.

3. Results and discussion

This section presents and discusses the results of the SSRT tests. First, the hydrogen-induced reduction in tensile properties is quantified for each test in terms of stress–strain curve, embrittlement index, and strain loss. Second, the fracture surfaces are analyzed to highlight the differences between drilled and reamed specimens, vintage and modern X65 steels, hydrogen and reference environments.

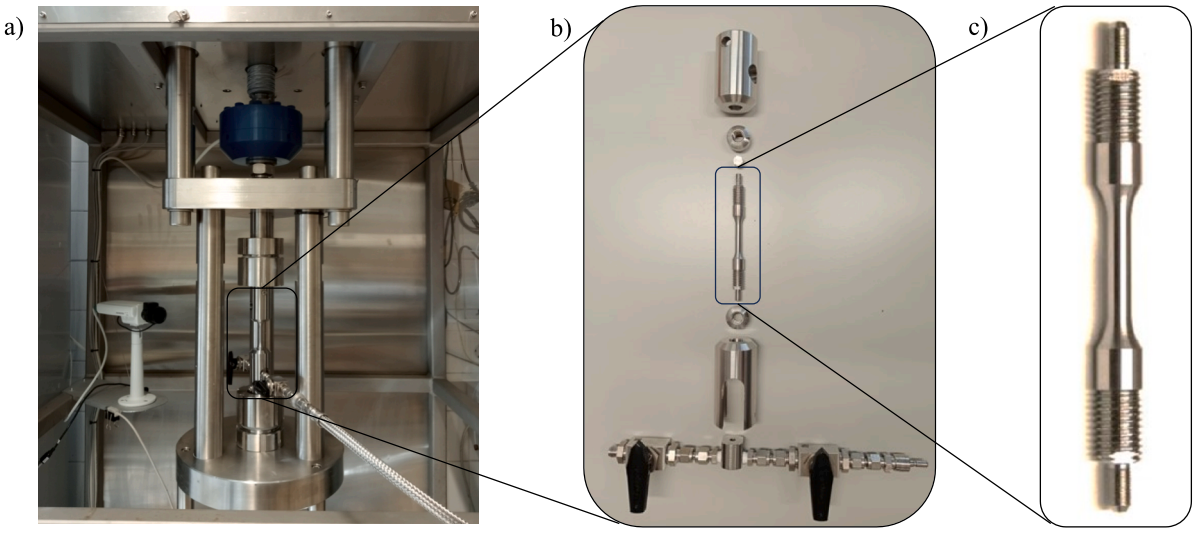

Fig. 3. Experimental setup for the a) SSRT tests, b) clamps and connections, and c) hollow specimen.

3.1. Hydrogen-induced reduction in tensile properties

The stress–strain curves for drilled and reamed specimens made of vintage and modern X65 pipeline steels are reported in Fig. 4 and Fig. 5, respectively. The following identification is used in the legend: V and M indicate the material, i.e., vintage or modern X65 steels; AR and H2 indicate the operating environment, i.e., argon or hydrogen gas; D and R indicate the surface finishing of the inner hole, i.e., drilled or reamed, and the numbers indicate the test repetition. For the tests in hydrogen atmosphere, drilled specimens are marked with red lines, reamed specimens with blue lines, whereas the reference tests in argon are drawn with black lines.

The tensile curves of the vintage X65 steel are unaffected by hydrogen up to the ultimate tensile strength. This observation is independent of the specimen's surface conditions. For this reason, it is assumed that the hydrogen atmosphere has a minimal impact on the yield strength and the ultimate tensile strength, which are substantially unaffected by the manufacturing process of the inner hole. Furthermore, the YS and UTS of this steel are not influenced by the presence of 60 bar gaseous hydrogen. These findings are consistent with those by Michler et al. [18] for a similar X60 pipeline steel. In contrast, all the specimens tested in H_2 gas exhibit a different mechanical behavior from the reference samples after reaching the maximum stress. The pressurized hydrogen induces a ductility loss, resulting in a lower strain at fracture, as reported by several studies [38–41] conducted on similar steels. It must be mentioned that the deviation of the strain at fracture is more significant for the samples tested in hydrogen than for the reference ones. In addition, the results of the drilled samples show a higher scattering than the reamed ones. Since almost no difference is observed for the tests in argon, the source of the scattering must be attributed to the hydrogen-metal interaction. It is well known that many environmental, material, and mechanical factors influence the susceptibility to HE; among them, stress concentration is one of the driving forces for hydrogen uptake and accumulation into the metal lattice. The higher inner surface roughness of the drilled specimens determines higher local stresses during tensile loading. As a result, hydrogen uptake is significantly enhanced in regions with high stress triaxiality, such as surface defects, thus influencing crack initiation and propagation. A secondary effect of notches, grooves, and scratches is related to the larger surface exposed to CGH_2, which may facilitate the adsorption and absorption of hydrogen atoms. In the case of drilled specimens, the significant scattering might be due to the limited control over the inner surface roughness, which has a comparatively higher influence on the tests conducted in hydrogen gas.

Based on the results of the vintage X65 steel tested in argon, which show how the stress–strain curves are not affected by the machining technique, reference tests with drilled and reamed specimens are considered comparable. Therefore, the reference tests for the modern X65 are performed with reamed samples only. Similarly to the results obtained on the vintage X65, the SSRT tests the drilled hollow specimens of modern X65 show a negligible influence of hydrogen up to the UTS, lower strain at fracture, and significant scattering. In contrast, the yield and ultimate tensile strength of modern reamed samples tested in hydrogen are slightly higher than those measured in reference atmosphere. According to the relatively small number of tests and considering that the samples were manufactured in two batches, the effect cannot be uniquely related to the presence of hydrogen. In addition, scattering in the results due to a slight shift of the extraction position might cause these differences, as confirmed by Venkatsurya et al. [42] for a similar pipeline steel.

Table 3 summarizes the results of the testing campaign. Yield and ultimate tensile strengths, reduced area at fracture, and strain at failure are measured for each test. In addition, the influence of the hydrogen environment is quantified in terms of embrittlement index and strain loss by comparing the reduced area and the strain at failure in H_2 with that in argon. The type of failure (either perpendicular or slanted with respect to the loading direction) and the test duration are specified for each test.

Fig. 6 shows the average embrittlement index (with solid bars) and strain loss (with striped bars) calculated for drilled and reamed

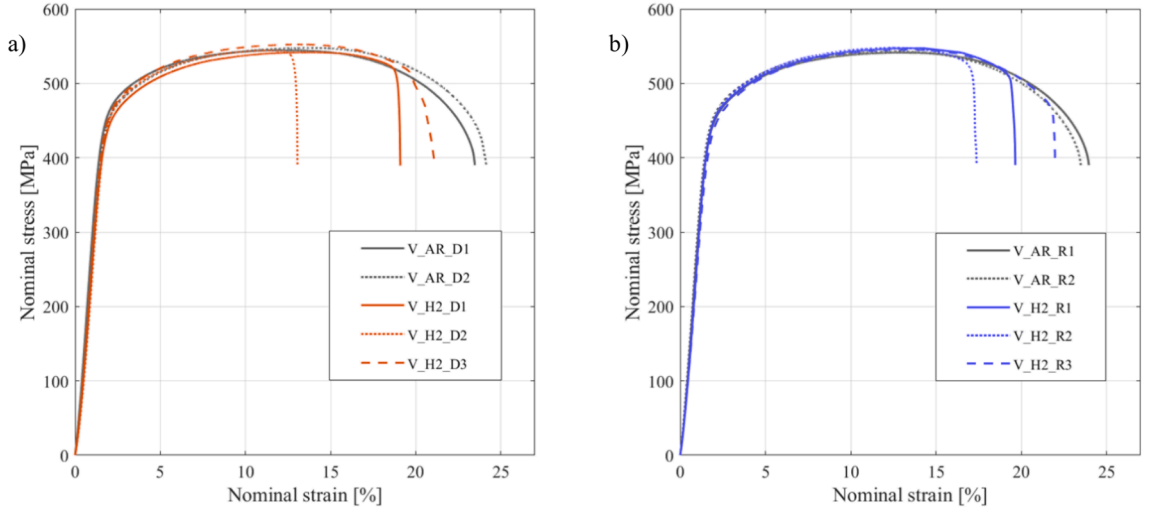

Fig. 4. Stress – strain curves of the vintage X65 for a) drilled specimens in Ar and H_2 (black and red lines, respectively), and b) reamed specimens in Ar and H_2 (black and blue lines, respectively). (For interpretation of the references to colour in this figure legend, the reader is referred to the web version of this article.)

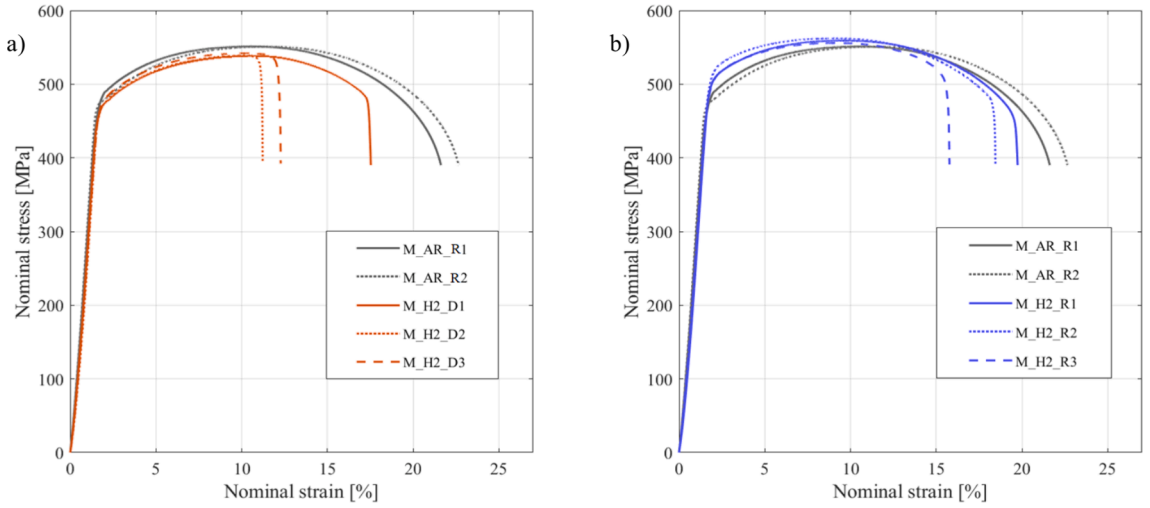

Fig. 5. Stress – strain curves of the modern X65 for a) drilled specimens in H_2 (red lines), and b) reamed specimens in Ar and H_2 (black and blue lines, respectively). (For interpretation of the references to colour in this figure legend, the reader is referred to the web version of this article.)

specimens of vintage and modern X65. The black bars indicate the error for each calculated value.

The results show how exposure to high-pressure hydrogen gas determines a significant strain loss in drilled specimens of vintage steel (i.e., 25.45 ± 17.70 %). The reduction of area is significantly lower for the specimens tested in hydrogen gas compared to the reference in argon, thus resulting in an EI of 28.19 ± 11.45 %. The measured strain at failure and the reduction of area features high scattering, which could result from the inhomogeneous microstructure of the vintage pipeline steel. Reamed specimens of vintage X65 show similar results in pressurized hydrogen gas, with a strain loss of 17.14 ± 9.80 % and an EI of 13.38 ± 9.14 %. In general, the results indicate how the mechanical properties of reamed specimens are less affected by hydrogen and have limited scattering compared to the drilled ones. In addition, they highlight a remarkable influence of the surface conditions on the hydrogen susceptibility of the component. It is evident that surface defects, such as notches and grooves resulting from the drilling process, can act as crack initiation sites and hydrogen concentrators, constituting preferential paths for hydrogen uptake into the bulk material, thus accelerating the failure. Interestingly, despite the different surface finishings, drilled and reamed specimens manifest comparable strain at failure and reduction of area when tested in argon. The average test duration reflects the trends observed for the strain at failure. It is the highest for the specimens tested in argon and lower in hydrogen environments, particularly for drilled specimens.

Qualitatively, the same observations can be made for the results obtained on the modern X65. The hydrogen-induced strain loss is 38.24 ± 15.39 % for drilled specimens and 18.78 ± 9.55 % for reamed ones, while the embrittlement indexes are 40.55 ± 13.72 % and 16.56 ± 13.88 % for drilled and reamed specimens, respectively. This makes it clear that the hydrogen-induced reduction in tensile properties is more prominent in drilled specimens for both tested steels. The average EI and ε_{loss} of the reamed specimens show that the reduction in mechanical properties is nearly equal for vintage and modern X65 steel. In contrast, the drilled specimens made of modern steel manifest higher average strain loss and EI than those made of vintage X65.

The observations regarding the average duration of the SSRT tests with vintage X65 also apply to modern steel. The latter shows an even more significant difference between drilled and reamed specimens tested in pressurized H_2. These findings might indicate a higher susceptibility to hydrogen embrittlement for modern steel. On the other hand, the scatter of the results must be considered. For both materials, the results are characterized by a significant standard deviation. In Fig. 4 and Fig. 5, two out of three tested samples of vintage X65 show a relatively low reduction of mechanical properties, and two out of three samples of modern steel show a remarkable hydrogen effect in terms of strain reduction. This observation is confirmed by the values reported in Table 3. Because of the relatively small number of samples, no clear conclusion can be drawn concerning a higher susceptibility to hydrogen embrittlement either for the vintage or the modern X65 steel.

3.2. *Fractographic analysis*

The fractographic analysis of a reamed specimen of vintage X65 tested in argon is shown in Fig. 7. The post-mortem cross-section is characterized by an elliptical shape (in Fig. 7a), revealing the anisotropic mechanical properties of the material. The topography of the fracture surface presents dimples (in Fig. 7b), indicating ductile microvoid coalescence (MVC). Necking is visible from the general view, and the fracture surface is perpendicular to the tensile direction. Similar elliptical fracture surfaces and MVC characterize the drilled specimens tested in argon at higher magnification. Notably, in one drilled specimen, the crack is slanted from the direction perpendicular to the applied load, thus revealing the possible presence of local inhomogeneities.

The fractographic analysis of drilled and reamed specimens of vintage X65 tested in compressed gaseous hydrogen are shown in Fig. 8 and Fig. 9, respectively. For those specimens, the post-mortem cross-section is elliptical (Fig. 8a and Fig. 9a). Due to the hydrogen-induced lowered strain at failure, the elliptical shape is less evident than in the reference samples. Moreover, it is possible to

Table 3
Results of the SSRT tests in hydrogen and argon for drilled and reamed specimens of vintage and modern X65 steels.

ID	Material	Type	Environment	YS [MPa]	UTS [MPa]	Reduction of area [%]	Embrittlement index [%]	Strain at failure [%]	Strain loss [%]	Type of failure	Test duration [h]
V_Ar_D1	Vintage X65	Drilled	6 MPa Ar	462.0	545.0	67.56	–	23.47	–	Perpendicular	65.63
V_Ar_D2	Vintage X65	Drilled	6 MPa Ar	453.0	548.0	65.62	–	24.15	–	Slanted	67.48
Average	**Vintage X65**	**Drilled**	**6 MPa Ar**	**457.5 ± 6.4**	**546.5 ± 2.1**	**66.59 ± 1.37**	–	**23.81 ± 0.48**	–	–	**66.56 ± 1.31**
V_H_2_D1	Vintage X65	Drilled	6 MPa H_2	443.0	542	46.78	29.75	19.10	19.78	Perpendicular	54.14
V_H_2_D2	Vintage X65	Drilled	6 MPa H_2	451.0	544	40.83	38.68	13.05	45.19	Perpendicular	36.98
V_H_2_D3	Vintage X65	Drilled	6 MPa H_2	456.0	552	55.85	16.12	21.11	11.34	Slanted	59.65
Average	**Vintage X65**	**Drilled**	**6 MPa H_2**	**450.0 ± 6.6**	**546.0 ± 5.3**	**47.82 ± 7.56**	**28.19 ± 11.45**	**17.75 ± 4.20**	**25.45 ± 17.70**	–	**50.26 ± 11.82**
V_Ar_R1	Vintage X65	Reamed	6 MPa Ar	459	541	66.94	–	23.97	–	Perpendicular	67.00
V_Ar_R2	Vintage X65	Reamed	6 MPa Ar	457	543	67.33	–	23.50	–	Perpendicular	65.74
Average	**Vintage X65**	**Reamed**	**6 MPa Ar**	**458.0 ± 1.41**	**542.0 ± 1.41**	**67.14 ± 0.28**	–	**23.74 ± 0.33**	–	–	**66.37 ± 0.89**
V_H_2_R1	Vintage X65	Reamed	6 MPa H_2	452	548	60.45	9.96	19.65	17.22	Perpendicular	55.68
V_H_2_R2	Vintage X65	Reamed	6 MPa H_2	452	547	51.19	23.75	17.38	26.79	Perpendicular	49.05
V_H_2_R3	Vintage X65	Reamed	6 MPa H_2	440	545	62.85	6.39	21.99	7.37	Slanted	62.09
Average	**Vintage X65**	**Reamed**	**6 MPa H_2**	**448.0 ± 6.9**	**546.6 ± 1.5**	**58.16 ± 6.13**	**13.38 ± 9.14**	**19.67 ± 2.31**	**17.14 ± 9.80**	–	**55.61 ± 6.52**
M_H_2_D1	Modern X65	Drilled	6 MPa H_2	474	539	54.83	24.94	17.54	20.81	Perpendicular	49.81
M_H_2_D2	Modern X65	Drilled	6 MPa H_2	474	539	36.08	50.61	11.23	49.30	Perpendicular	31.71
M_H_2_D3	Modern X65	Drilled	6 MPa H_2	489	542	39.39	46.08	12.28	44.56	Perpendicular	34.63
Average	**Modern X65**	**Drilled**	**6 MPa H_2**	**479.0 ± 8.7**	**540.0 ± 1.7**	**43.43 ± 10.01**	**40.55 ± 13.72**	**13.68 ± 3.38**	**38.24 ± 15.39**	–	**38.72 ± 9.72**
M_Ar_R1	Modern X65	Reamed	6 MPa Ar	489	551	73.58	–	21.63	–	Slanted	60.52
M_Ar_R2	Modern X65	Reamed	6 MPa Ar	479	551	72.52	–	22.66	–	Slanted	63.36
Average	**Modern X65**	**Reamed**	**6 MPa Ar**	**484.0 ± 7.1**	**551.0**	**73.05 ± 0.75**	–	**22.15 ± 0.73**	–	–	**61.94 ± 2.01**
M_H_2_R1	Modern X65	Reamed	6 MPa H_2	505	559	69.66	4.64	19.75	10.84	Slanted	55.79
M_H_2_R2	Modern X65	Reamed	6 MPa H_2	515	562	63.34	13.29	18.45	16.70	Slanted	52.13
M_H_2_R3	Modern X65	Reamed	6 MPa H_2	504	556	49.84	31.77	15.77	28.80	Perpendicular	45.11
Average	**Modern X65**	**Reamed**	**6 MPa H_2**	**508.0 ± 6.1**	**559.0 ± 3.0**	**60.95 ± 10.12**	**16.56 ± 13.88**	**17.99 ± 2.03**	**18.78 ± 9.55**	–	**51.01 ± 5.43**

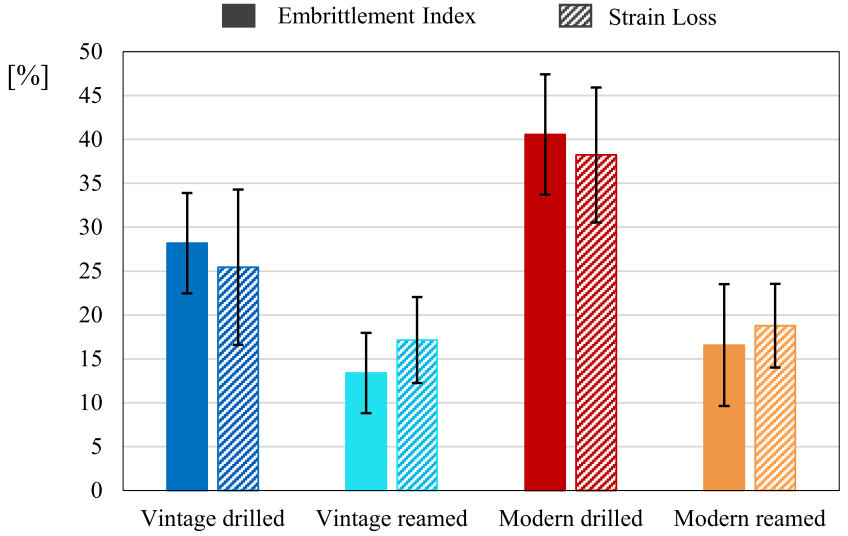

Fig. 6. Average embrittlement indexes and strain losses with standard deviations for drilled or reamed specimens made of vintage and modern X65.

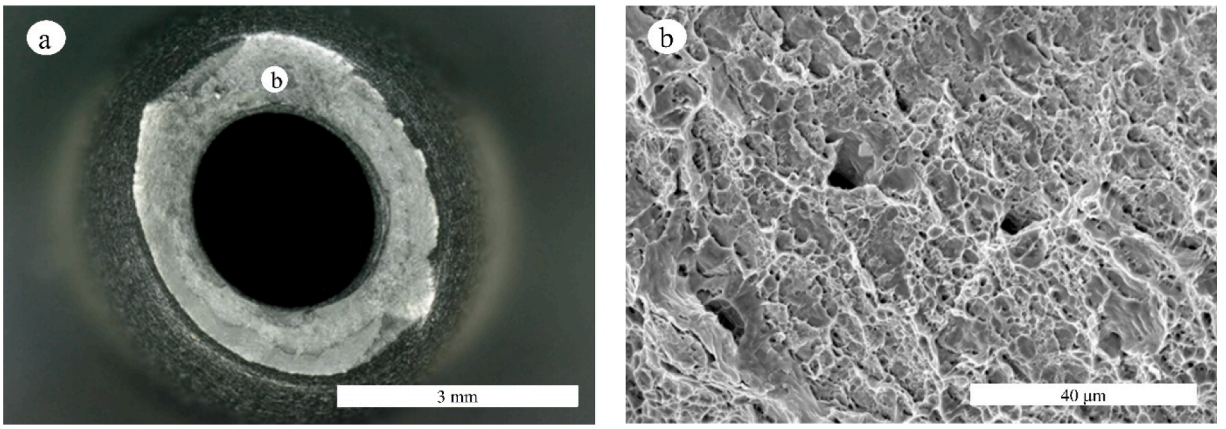

Fig. 7. Fractographic analysis of the vintage X65 for the reamed specimen tested in 6 MPa Ar a) in a general view and b) in a higher magnification.

distinguish three different areas when moving from the inner to the outer surface of the hollow specimen: a brittle quasi-cleavage region (QC), a brittle-to-ductile (BD) transition region, and a ductile region characterized by dimples. Similar observations were obtained on the same material when tested with conventional solid specimens under in-situ electrochemical charging. The area closer to the source of hydrogen was characterized by cleavage behavior, while the ductile behavior was increasingly prominent, moving towards the inner part of the specimen [43].

In the case of hollow specimens, the area near the inner surface is characterized by transgranular brittle fracture, as shown in Fig. 8b and Fig. 9b. This region, where signs of hydrogen-assisted fracture are evident, occupies a large portion of the fracture surface of the drilled specimens. The surface characterized by quasi-cleavage fracture is significantly lower in reamed specimens. Notably, the QC area has a different appearance in drilled and reamed samples, most likely due to the differences in the crack initiation behavior of these two specimen types. It can be speculated that the higher roughness inherent to the drilling process results in a higher number of local crack initiation sites. Multiple cracks are simultaneously initiated on the inner surface of the drilled specimens. The elevated local stress concentration in these regions fosters the hydrogen uptake into the metal bulk and might determine a more homogeneous concentration of H atoms in the inner annulus of the cross-section. In contrast, the fracture seems to be mainly driven by the formation and propagation of a single dominant crack starting from the internal surface of the reamed specimens. The crack tip has high localized stress and is a preferential site for hydrogen uptake. As a result, H atoms distribute unevenly throughout the specimen's cross-section and are primarily concentrated in the crack propagation direction. This difference could result in a different appearance of the quasi-cleavage zone of the drilled and reamed specimens.

The MVC region is limited to a small annulus at the outer surface of the drilled specimen in Fig. 8d, while it occupies a greater area of the fracture surface of the reamed specimen in Fig. 9d. This region is dominated by dimples, which appear deeper than those observed in the reference samples. The area between QC and MVC regions presents mixed features (Fig. 8c and Fig. 9c). Considering all

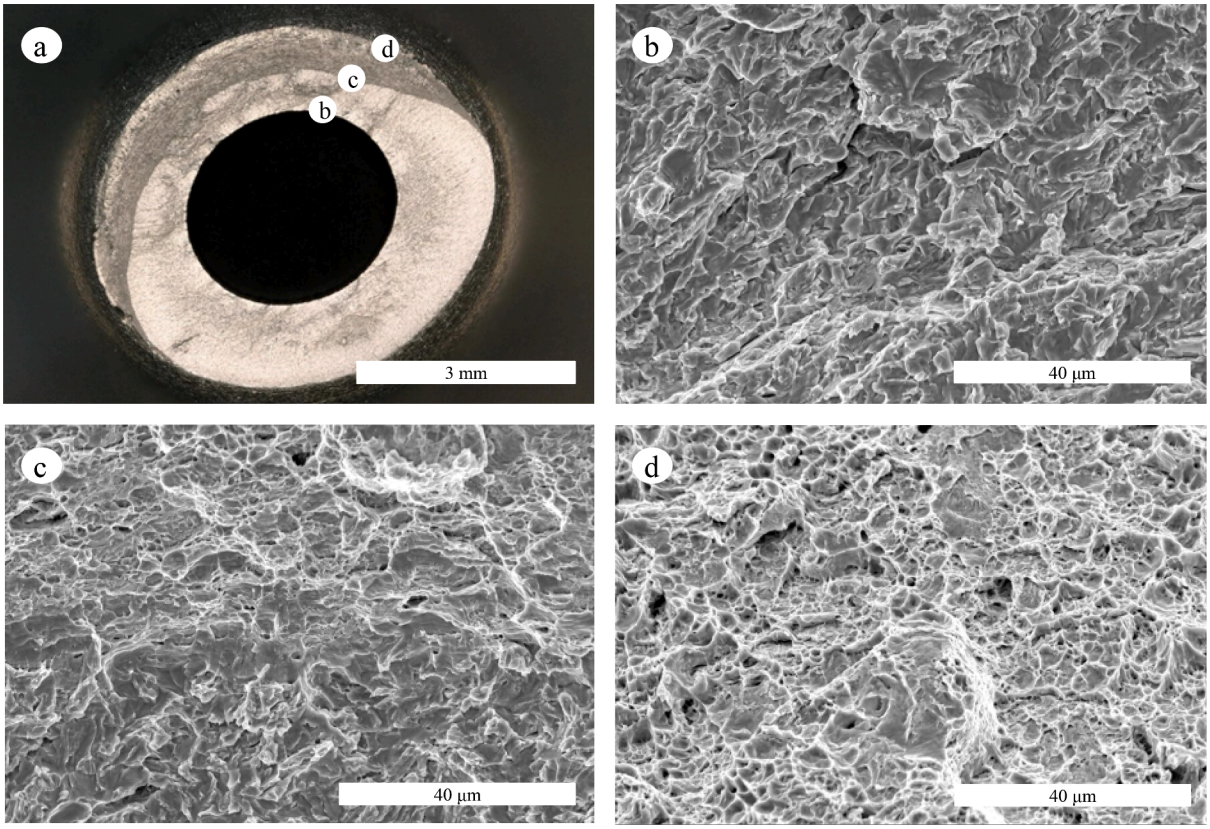

Fig. 8. Fractographic analysis of the vintage X65 for a drilled specimen tested in 6 MPa H_2. Higher magnifications of b) the brittle QC area, c) the transition BD area, and d) the ductile MVC area.

the tests conducted in hydrogen, the specimens show a significant scattering in the ratio between H_2-affected and unaffected zones. This observation correlates with the embrittlement index values: the larger the brittle area, the higher the corresponding EI will be. In most cases, the crack propagation is not concentric to the longitudinal axis of the specimens. Therefore, the crack penetrates the wall at a local spot, determining the hydrogen release and a sudden pressure drop within the hole. As hydrogen is released from the containment volume, the driving force for hydrogen uptake (i.e., the pressure) is lost, and the same magnitude of adsorption is impossible [33]. In most of the specimens tested in hydrogen, the topography of the fracture is perpendicular to the tensile direction. In some cases, the main hydrogen-assisted crack deviated from the expected direction perpendicular to the load, revealing the possible presence of local inhomogeneities of the banded microstructure. The specimens with slanted cracks tend to have longer test durations and show more necking from the outer diameter, higher strain at failure, and lower embrittlement index. This effect was also observed by Michler et al. [18] for X60 steel with similar microstructure.

The fractographic analysis of a reamed specimen of modern X65 tested in argon is shown in Fig. 10 in a general view and higher magnification. The reamed specimen's overview picture clearly shows the necking of the sample. The shape of the post-mortem cross-section is a nearly concentric ring. This is a clear difference in comparison to the elliptical shape observed on the vintage specimens in Fig. 7, which points out the difference in microstructure homogeneity between the two materials investigated. The dimples shown in the center of the SEM picture indicate the material's ductile behavior. Out of the center, a smeared surface generated by the slip of the sample halves during the test is visible.

Fig. 11 shows the fractographic images of the drilled sample of modern X65 tested in hydrogen. The appearance is similar to that of the drilled samples of the vintage X65 tested under the same conditions. As well as for the vintage steel, the fracture surface is divided into three different regions, namely the brittle QC zone (Fig. 11b), the transition BD zone (Fig. 11c), and the ductile zone, where dimples are dominant (Fig. 11d). Similarly to the fractographic surfaces of the drilled samples made from the vintage X65, these regions are characterized by the same fracture modes: a quasi-cleavage fracture in the brittle zone and microvoid coalescence in the ductile region. In contrast with vintage steel, the BD zone occupies a comparatively small surface, and there is a more abrupt transition between brittle and ductile fracture modes. The dimples in the MVC region indicate the material's ductile behavior. The origin of the voids is most likely due to local inhomogeneities in the material, such as the precipitates visible in Fig. 11c and Fig. 11d. This inhomogeneities tend to locally weaken the material, while the surrounding matrix maintains its integrity. In addition, the crack propagation is not concentric in the case of drilled samples of modern X65 tested in hydrogen atmospheres. Therefore, the crack penetrates the wall at a local spot, leading to the hydrogen release and a sudden pressure drop, which determines the formation of the

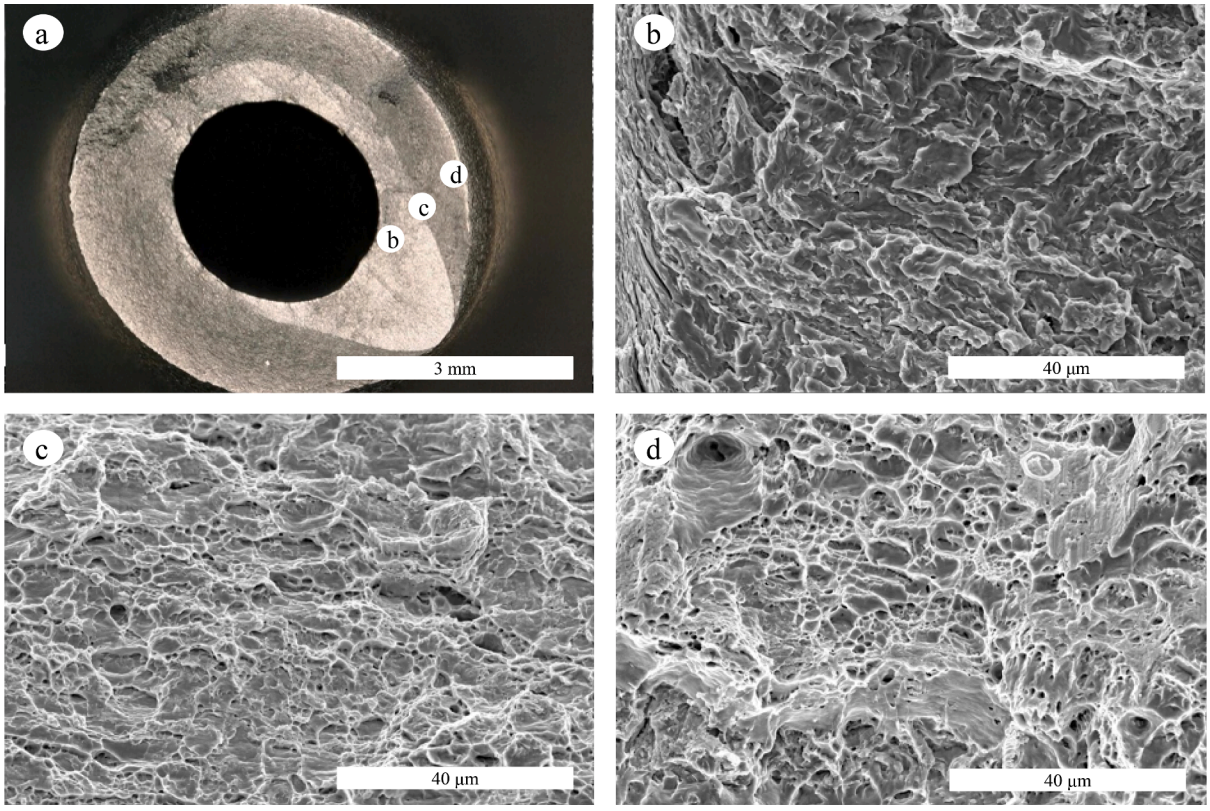

Fig. 9. Fractographic analysis of the vintage X65 for reamed specimen tested in 6 MPa H_2. Higher magnifications of b) the brittle QC area, c) the transition BD area, and d) the ductile MVC area.

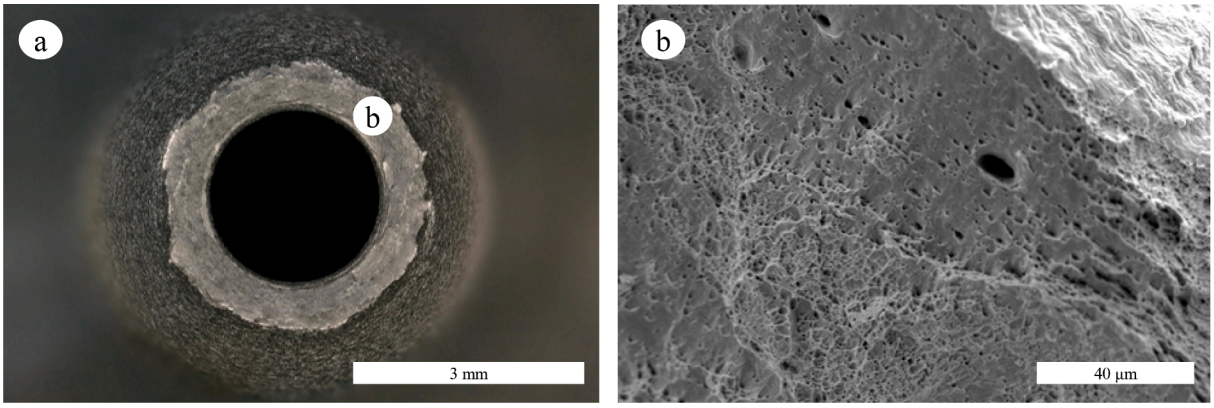

Fig. 10. Fractographic analysis of the modern X65 for the reamed specimen tested in 6 MPa Ar a) in a general view and b) in a higher magnification.

ductile annulus. This behavior is similar to that observed for the reference samples of vintage X65. All the drilled specimens fractured perpendicularly to the tensile direction.

The fractographic images of the reamed specimen made from modern steel and tested in hydrogen are shown in Fig. 12. The appearance is slightly different from the other configurations tested in hydrogen. There is no clear differentiation between the three regions. The overview picture (in Fig. 12a) shows a homogeneous appearance of the fracture surface. In addition, the SEM pictures with higher magnification highlight a slightly different material behavior. While the other configurations manifest a relatively plane QC fracture, the reamed sample of modern steel is characterized by a more scaly appearance (as shown in Fig. 12b and Fig. 12c). Compared to the fracture surface of the reamed sample tested in the reference atmosphere (in Fig. 10), the change in the fracture mode is clearly due to the presence of hydrogen. Nevertheless, also for the reamed sample of modern X65, there is a visible ductile region in the high-resolution SEM picture in Fig. 12d. This ductile zone is characterized by MVC fracture, as in the case of the other samples

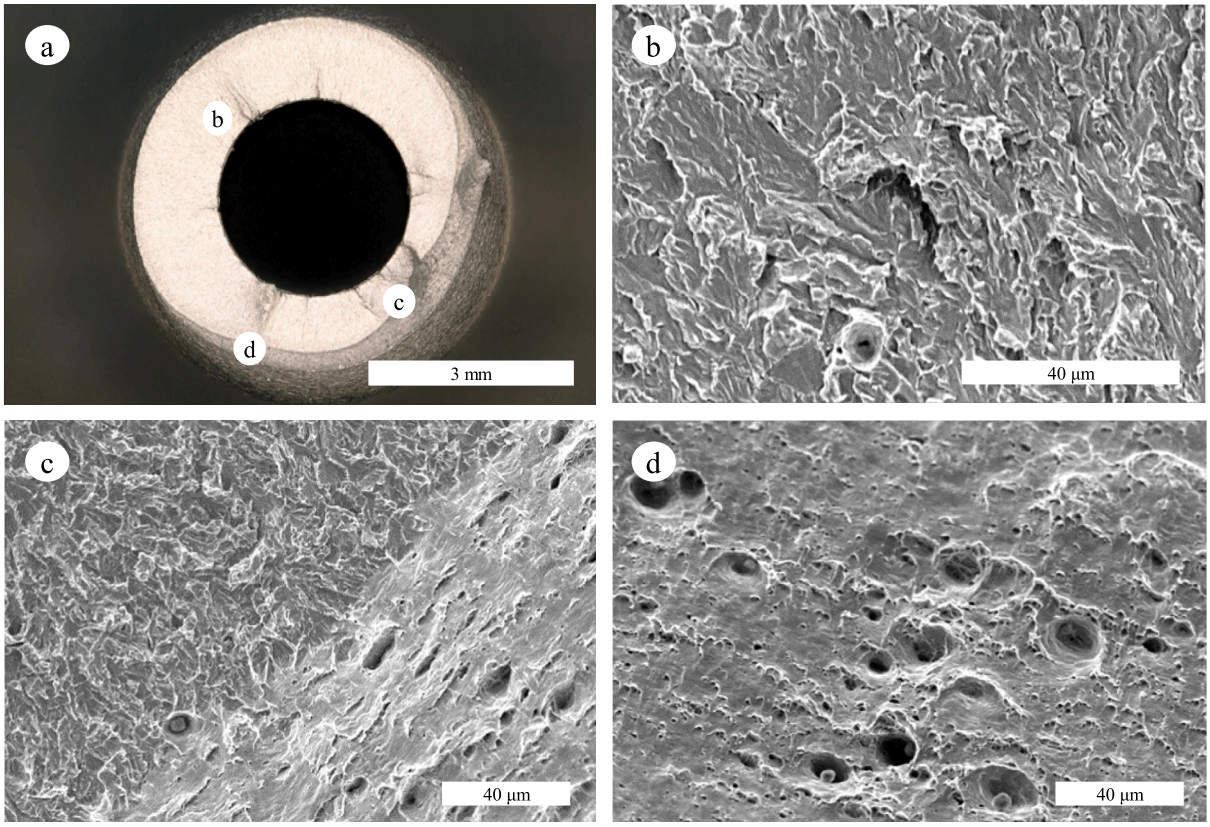

Fig. 11. Fractographic analysis of the modern X65 for drilled specimen tested in 6 MPa H_2. Higher magnifications of b) the brittle QC area, c) the transition BD area, and d) the ductile MVC area.

tested in hydrogen. Two of three reamed specimens exhibit a slanted fracture. These samples have higher EI and strain loss than the specimen fractured perpendicularly to the tensile direction. This is coherent with the considerations expressed for the vintage steel.

The permeation of hydrogen from the inner surface to local areas ahead of crack tips is essential in hydrogen-assisted cracking. The transport of H atoms can be either due to the diffusion through interstitial sites in the metal lattice or the dislocation mobility. Koren et al. [44] investigated the hydrogen diffusivity in the same vintage X65 tested in this study and similar modern steel, obtaining high diffusion coefficients (2.70×10^{-10} to 3.34×10^{-10} m^2/s for vintage and modern steels, respectively) and significant scattering for the vintage steel due to the presence of major traps and ferrite-pearlite bands. In addition, it is well-known that hydrogen transport by dislocations plays a crucial role during plastic deformation [45]. Considering that all the specimens exposed to CGH_2 failed after necking was initiated, it may be argued that transport by dislocation mobility is also responsible for solubilizing hydrogen and influences the ductility reduction at the macroscopic level.

The post-mortem analysis of the inner surface shows significant differences between drilled and reamed specimens. The typical drilled hole surface is characterized by evident scratches enveloping large sections characterized by "smooth" areas, probably due to chip removal during manufacturing. In contrast, the reamed hole surface does not exhibit any visible scratch or imperfection. Notably, the average ten-point height of irregularities is six times lower in reamed specimens than in drilled ones (R_z is 1.4 and 8.5 μm, respectively). A thorough analysis of the necked region does not show preferred cracking from the scratches due to the high ductility of the X65 steel. The main difference between drilled and reamed specimens pertains to multiple cracks in the surface exposed to H_2 gas. These cracks can be observed in the necking zone of the reamed specimens. In contrast, they are present in the necked region and the zone far from the fracture (i.e., the area characterized by uniform plastic deformation) of the drilled specimens. This difference in the crack distribution between drilled and reamed specimens cannot be observed in the specimens tested in argon, thus confirming the influence of the inner surface roughness on the degradation in tensile properties in hydrogen environments.

4. Conclusions

Failures of pipeline systems can have severe environmental, human, and economic consequences. Therefore, ensuring the physical integrity of such systems is paramount. This study, which delves into the tensile properties of API 5L X65 steel under high-pressure hydrogen conditions, is a significant step in this direction. The investigation, conducted through tensile testing with hollow specimens, compares two types of specimens to assess the impact of inner surface roughness on crack initiation and propagation. The key

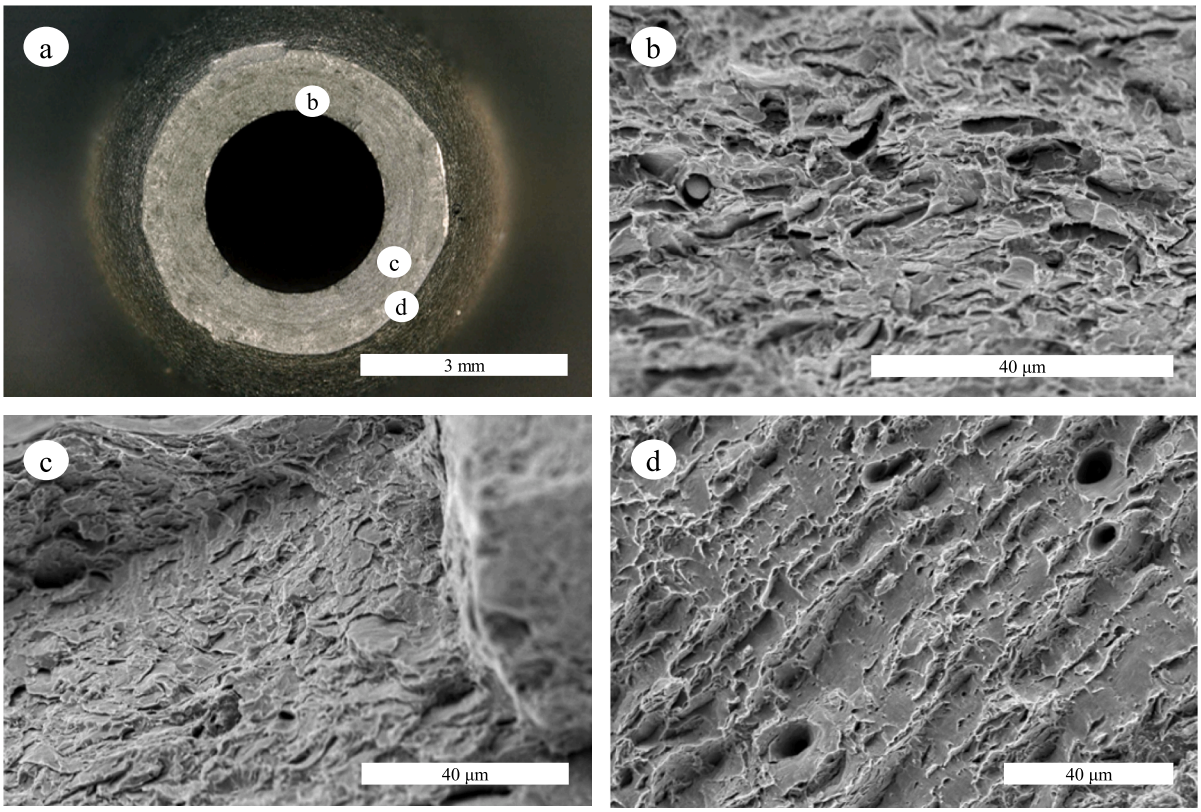

Fig. 12. Fractographic analysis of the modern X65 for reamed specimen tested in 6 MPa H_2. Higher magnifications of b) brittle QC area, c) the transition BD area and d) the ductile MVC area.

findings are as follows:

- The tensile properties of vintage and modern X65 were significantly degraded in pressurized hydrogen gas, proving the pipeline steel's susceptibility to hydrogen embrittlement.
- The level of surface finishing investigated did not substantially impact the tensile properties in inert environments. In contrast, drilled specimens exhibited lower strain at failure and reduction of area than reamed ones in pressurized hydrogen gas and showed greater scatter in the results.
- The crack propagation is not concentric to the longitudinal axis of the samples and penetrates the wall at a local spot. This effect is more prominent for the vintage X65, which shows anisotropic mechanical properties, even for the tests in reference atmosphere. It is most likely due to its banded microstructure resulting from manufacturing.
- The post-mortem analysis showed the presence of a hydrogen-affected region close to the inner wall of the specimen, a micro-void coalescence region close to the outer wall, and a transition area in between. This observation was consistent for all the specimens tested in H_2 gas, regardless of the age and manufacturing process of the material.

The results of this study underscore the importance of considering the evolution of surface conditions when assessing the HE susceptibility of non-notched or cracked components for hydrogen transport and storage. However, a direct comparison between hollow and conventional specimens is necessary to fully understand the hydrogen effect on the tensile properties of the materials. In particular, the similarities and differences in the stress–strain evolution need to be carefully assessed. Eventual differences in the stress state between conventional and hollow specimens affect and are affected by hydrogen ingress and distribution in the specimen cross-section. This aspect becomes even more relevant when necking begins (i.e. when hydrogen effects become evident at the macroscale level). Consequently, different stress–strain state evolution inherent to the specimen geometries may play an essential role in the magnitude of ductility loss. While this investigation demonstrates the potential to assess HE susceptibility using hollow specimens, further research is crucial to standardize this technique and enable direct comparisons with the autoclave tests. Moreover, the reduction in the tensile properties of structural materials should be tackled through preventive maintenance strategies, particularly as we consider blending higher fractions of hydrogen into the existing pipelines. Therefore, a tailored integrity management approach for hydrogen pipelines could include detecting and identifying defects through in-line inspections, developing damage prediction models based on inspection data, and estimating the probabilities of failure. By implementing predictive maintenance strategies for hydrogen transport pipelines, we can significantly reduce the frequency of equipment breakdowns and unintended hazardous releases.

CRediT authorship contribution statement

Alessandro Campari: Writing – review & editing, Writing – original draft, Visualization, Methodology, Investigation, Formal analysis, Data curation, Conceptualization. **Florian Konert:** Writing – review & editing, Writing – original draft, Visualization, Methodology, Investigation, Formal analysis, Conceptualization. **Oded Sobol:** Writing – review & editing, Supervision, Resources, Funding acquisition. **Antonio Alvaro:** Writing – review & editing, Supervision, Resources, Funding acquisition.

Declaration of competing interest

The authors declare that they have no known competing financial interests or personal relationships that could have appeared to influence the work reported in this paper.

Data availability

Data will be made available on request.

Acknowledgments

This work was undertaken as a part of the research projects SH_2IFT – 2 (Safe hydrogen fuel handling and use for efficient implementation 2) and FME HYDROGENi (Norwegian research and innovation centre for hydrogen and ammonia), and the authors would like to acknowledge the financial support of the Research Council of Norway (Grant No. 327009 and 333118).

References

[1] European Commission, Hydrogen strategy for a climate-neutral Europe, COM(2020) 301 (2020). https://energy.ec.europa.eu/system/files/2020-07/hydrogen_strategy_0.pdf.
[2] A. Campari, A.J. Nakhal Akel, F. Ustolin, A. Alvaro, A. Ledda, P. Agnello, P. Moretto, R. Patriarca, N. Paltrinieri, Lessons learned from HIAD 2.0: Inspection and maintenance to avoid hydrogen-induced material failures, Comput. Chem. Eng. 173 (2023) 108199, https://doi.org/10.1016/j.compchemeng.2023.108199.
[3] J. Cao, Effect of hydrogen embrittlement on the safety assessment of low-strength hydrogen transmission pipeline, Eng. Fail. Anal. 156 (2024) 107787, https://doi.org/10.1016/j.engfailanal.2023.107787.
[4] J.A. Lee, Hydrogen embrittlement NASA/TM-2016-218602, 2016.
[5] E. Ohaeri, U. Eduok, J. Szpunar, Relationship between microstructural features in pipeline steel and hydrogen assisted degradation, Eng. Fail. Anal. 96 (2019) 496–507, https://doi.org/10.1016/j.engfailanal.2018.11.008.
[6] A. Campari, F. Ustolin, A. Alvaro, N. Paltrinieri, A review on hydrogen embrittlement and risk- based inspection of hydrogen technologies, Int. J. Hydrogen Energy 48 (2023) 35316–35346, https://doi.org/10.1016/j.ijhydene.2023.05.293.
[7] M.A. Mohtadi-Bonab, M. Masoumi, J.A. Szpunar, A comparative fracture analysis on as-received and electrochemically hydrogen charged API X60 and API X60SS pipeline steels subjected to tensile testing, Eng. Fail. Anal. 129 (2021) 105721, https://doi.org/10.1016/j.engfailanal.2021.105721.
[8] M.B. Djukic, G.M. Bakic, V. Sijacki Zeravcic, A. Sedmak, B. Rajicic, The synergistic action and interplay of hydrogen embrittlement mechanisms in steels and iron: Localized plasticity and decohesion, Eng. Fract. Mech. 216 (2019) 106528, https://doi.org/10.1016/j.engfracmech.2019.106528.
[9] ASME International, ASME B31.12 - Hydrogen Piping and Pipelines, 2019.
[10] ASME, ASME BPVC Section VIII - Rules for Construction of Pressure Vessels Division 3 - Alternative Rules for Construction of High Pressure Vessels, 2023.
[11] DNV, DNV-ST-F101 - Submarine pipeline systems, 2021.
[12] J. Zhang, Y.F. Cheng, Modeling of hydrogen atom distribution at corrosion defect on existing pipelines repurposed for hydrogen transport under pressure fluctuations, Int. J. Hydrogen Energy 58 (2024) 1075–1087, https://doi.org/10.1016/j.ijhydene.2024.01.213.
[13] J. Zhang, Y.F. Cheng, Numerical analysis of hydrogen atom diffusion and trapping at an unconstrained dent on pipelines, Int. J. Press. Vessel. Pip. 206 (2023) 105032, https://doi.org/10.1016/j.ijpvp.2023.105032.
[14] C. San Marchi, B.P. Somerday, SANDIA REPORT Technical Reference for Hydrogen Compatibility of Materials, 2012.
[15] Y. Zhao, M.Y. Seok, I.C. Choi, Y.H. Lee, S.J. Park, U. Ramamurty, J.Y. Suh, J. Il Jang, The role of hydrogen in hardening/softening steel: Influence of the charging process, Scr. Mater. 107 (2015) 46–49, https://doi.org/10.1016/j.scriptamat.2015.05.017.
[16] ASTM International, G142–98 Standard Test Method for Determination of Susceptibility of Metals to Embrittlement in Hydrogen Containing Environments at High Pressure, High Temperature, or both (2022).
[17] ISO, ISO 11114-4 Transportable gas cylinders - Compatibility of cylinder and valve materials with gas contents - Part 4: Test methods for selecting steels resistant to hydrogen embrittlement, 2017.
[18] T. Michler, F. Ebling, H. Oesterlin, C. Fischer, K. Wackermann, Comparison of tensile properties of X60 pipeline steel tested in high pressure gaseous hydrogen using tubular and conventional specimen, Int. J. Hydrogen Energy 47 (2022) 34676–34688, https://doi.org/10.1016/j.ijhydene.2022.07.211.
[19] T. Michler, F. Ebling, Influence of high pressure hydrogen upon the tensile properties of selected pressure vessel and pipeline steels, (2021).
[20] T. Ogata, Evaluation of Hydrogen Embrittlement by Internal High-Pressure Hydrogen Environment in Specimen, J. Japan Inst. Met. Mater. 72 (2008) 125–131, https://doi.org/10.2320/jinstmet.72.125.
[21] T. Ogata, Hydrogen embrittlement evaluation in tensile properties of stainless steels at cryogenic temperatures, AIP Conf. Proc. (2008) 124–131, https://doi.org/10.1063/1.2900335.
[22] T. Ogata, Hydrogen environment embrittlement evaluation in fatigue properties of stainless steel SUS304L at cryogenic temperatures, AIP Conf. Proc. (2010) 25–32, https://doi.org/10.1063/1.3402310.
[23] T. Ogata, Influence of high pressure hydrogen environment on tensile and fatigue properties of stainless steels at low temperatures, AIP Conf. Proc. (2012) 39–46, https://doi.org/10.1063/1.4712078.
[24] T. Ogata, Hydrogen Environment Embrittlement on Austenitic Stainless Steels from Room Temperature to Low Temperatures, IOP Conf. Ser.Mater. Sci. Eng. (2015) 1–8, https://doi.org/10.1088/1757-899X/102/1/012005.
[25] A. Ueno, G. Benjamin, Effect of high-pressure H2 gas on tensile and fatigue properties of stainless steel SUS316L by means of the internal high-pressure H2 gas method, Procedia Struct. Integr. 19 (2019) 494–503, https://doi.org/10.1016/j.prostr.2019.12.053.
[26] T. Ogata, , Influence of 70 MPa hydrogen gas on SUS 630 from 77 K to 373 K by simple testing method, Proc. ASME 2009 Press. Vessel. Pip. Conf. (2018) 1–5, doi:10.1115/pvp2018-84462.
[27] T. Ogata, Simple mechanical testing method to evaluate influence of high pressure hydrogen gas, Proc. ASME 2018 Press. Vessel. Pip. Conf. (2018) 1–9, doi:10.1115/pvp2018-84187.

[28] T. Ogata, Y. Ono, Influence of roughness of inner surface of simple mechanical testing method to evaluate influence of high pressure hydrogen gas, Proc. ASME 2019 Press. Vessel. Pip. Div. Conf. (2019) 1–6, doi:10.1115/PVP2019-93492.
[29] T. Michler, T. Freitas, H. Oesterlin, C. Fischer, K. Wackermann, F. Ebling, Tensile testing in high pressure gaseous hydrogen using conventional and tubular specimens: Austenitic stainless steels, Int. J. Hydrogen Energy 48 (2023) 25609–25618, https://doi.org/10.1016/j.ijhydene.2023.03.248.
[30] T. Boot, T.A.C. Riemslag, E.T.E. Reinton, P. Liu, C.L. Walters, V. Popovich, In-situ hollow sample setup design for mechanical characterisation of gaseous hydrogen embrittlement of pipeline steels and welds, Metals (Basel). 11 (2021), https://doi.org/10.3390/met11081242.
[31] L.E. Faucon, T. Boot, T. Riemslag, S.P. Scott, P. Liu, V. Popovich, Hydrogen-Accelerated Fatigue of API X60 Pipeline Steel and Its Weld, Metals (Basel). 13 (2023) 1–20, https://doi.org/10.3390/met13030563.
[32] F. Konert, F. Wieder, J. Nietzke, D. Meinel, B. Thomas, Evaluation of the Impact of Gaseous Hydrogen on Pipeline Steels Utilizing Hollow Specimen Technique and μCT 59 (2024) 874–879, https://doi.org/10.1016/j.ijhydene.2024.02.005.
[33] F. Konert, A. Campari, J. Nietzke, O. Sobol, A. Alvaro, Evaluation of the tensile properties of X65 pipeline steel in compressed gaseous hydrogen using hollow specimens, Procedia Struct. Integr. 54 (2024) 204–211, https://doi.org/10.1016/j.prostr.2024.01.074.
[34] G. Pluvinage, Mechanical properties of a wide range of pipe steels under influence of pure hydrogen or hydrogen blended with natural gas, Int. J. Press. Vessel. Pip. 190 (2021) 104293, https://doi.org/10.1016/j.ijpvp.2020.104293.
[35] A.O. Myhre, A.B. Hagen, B. Nyhus, V. Olden, A. Alvaro, A. Vinogradov, Hydrogen Embrittlement Assessment of Pipeline Materials Through Slow Strain Rate Tensile Testing, Procedia Struct. Integr. 42 (2022) 935–942, https://doi.org/10.1016/j.prostr.2022.12.118.
[36] API, API 5L - Line Pipe, 2018.
[37] ANSI, ANSI/CSA CHMC 1-2014 - Test Methods For Evaluating Material Compatibility In Compressed Hydrogen Applications - Metals, 2014.
[38] Y.H. Lee, H.M. Lee, Y. Il Kim, S.H. Nahm, Mechanical degradation of API X65 pipeline steel by exposure to hydrogen gas, Met. Mater. Int. 17 (2011) 389–395, https://doi.org/10.1007/s12540-011-0614-1.
[39] D. Wang, A.B. Hagen, P.U. Fathi, M. Lin, R. Johnsen, X. Lu, Investigation of hydrogen embrittlement behavior in X65 pipeline steel under different hydrogen charging conditions, Mater. Sci. Eng. A 860 (2022), https://doi.org/10.1016/j.msea.2022.144262.
[40] M. Ranjbar, R. Miresmaeili, M.R. Naimi-Jamal, M. Mirzaei, Effect of Microstructure on the Mechanical Properties and Fracture Toughness of API X65 Pipeline Steel in the Presence of Hydrogen, Met. Mater. Int. 27 (2021) 3918–3934, https://doi.org/10.1007/s12540-020-00882-8.
[41] R. Khatib Zadeh Davani, R. Miresmaeili, M. Soltanmohammadi, Effect of thermomechanical parameters on mechanical properties of base metal and heat affected zone of X65 pipeline steel weld in the presence of hydrogen, Mater. Sci. Eng. A 718 (2018) 135–146, https://doi.org/10.1016/j.msea.2018.01.101.
[42] P.K.C. Venkatsurya, Z. Jia, R.D.K. Misra, M.D. Mulholland, M. Manohar, J.E. Hartmann, Understanding mechanical property anisotropy in high strength niobium-microalloyed linepipe steels, Mater. Sci. Eng. A 556 (2012) 194–210, https://doi.org/10.1016/j.msea.2012.06.078.
[43] M. Lin, H. Yu, D. Wang, A. Díaz, A. Alvaro, V. Olden, E. Koren, Y. Ding, J. He, Z. Zhang, Experimental and numerical study on hydrogen-induced failure of X65 pipeline steel, Mater. Sci. Eng. A 894 (2024), https://doi.org/10.1016/j.msea.2024.146175.
[44] E. Koren, J. Yamabe, X. Lu, C.M.H. Hagen, D. Wang, R. Johnsen, Hydrogen diffusivity in X65 pipeline steel: Desorption and permeation studies, Int. J. Hydrogen Energy 61 (2024) 1157–1169, https://doi.org/10.1016/j.ijhydene.2024.03.027.
[45] J. Tien, A.W. Thompson, I.M. Bernstein, R.J. Richards, Hydrogen transport by dislocations, Metall. Trans. A 7 (1976) 821–829, https://doi.org/10.1007/BF02644079.